

1 The Influence of Lateral Earth Structure on Inferences of Global Ice Volume During the Last  
2 Glacial Maximum

3 Linda Pan<sup>1\*</sup>, Glenn A. Milne<sup>2</sup>, Konstantin Lamychev<sup>1</sup>, Samuel L. Goldberg<sup>3</sup>, Jacqueline  
4 Austermann<sup>4</sup>, Mark J. Hoggard<sup>5</sup>, Jerry X. Mitrovica<sup>1</sup>.

5 <sup>1</sup>Department of Earth and Planetary Sciences, Harvard University.

6 <sup>2</sup>Department of Earth and Environmental Sciences, University of Ottawa.

7 <sup>3</sup>Department of Earth, Atmospheric and Planetary Sciences, Massachusetts Institute of  
8 Technology.

9 <sup>4</sup>Lamont-Doherty Earth Observatory, Columbia University.

10 <sup>5</sup>Research School of Earth Sciences, Australian National University.

11 \*Corresponding author

12 Email: [lindapan@g.harvard.edu](mailto:lindapan@g.harvard.edu).

13 Mailing address: Department of Earth and Planetary Sciences, 20 Oxford St.,  
14 Cambridge, MA 02138

15 Keywords: Last Glacial Maximum; Sea-level change; Glacial isostatic adjustment; Global ice  
16 volume; Numerical modeling

17

18 **Abstract**

19           The mapping between far-field relative sea level (RSL) records and changes in ice  
20 volume or global mean sea level (GMSL) involves a correction for glacial isostatic adjustment  
21 (GIA). This mapping is thus sensitive to uncertainties inherent to GIA modeling, including the  
22 spatio-temporal history of ice mass changes and viscoelastic Earth structure. Here, we investigate  
23 the effect of incorporating lateral variations in Earth structure on predicting far-field sea level in  
24 order to determine if this source of model uncertainty significantly impacts estimates of global  
25 ice volume at the Last Glacial Maximum (LGM). We consider a set of forty 3-D simulations that  
26 sample different Earth model parameters: the adopted lithospheric thickness, the seismic velocity  
27 model used to infer lateral temperature variations, the scaling factor used in the conversion from  
28 temperature to viscosity, and the spherically averaged “background” viscosity profile. In  
29 addition, we consider results based on two ice histories. We present global maps of the  
30 differences between these simulations and a set of 1-D simulations at the LGM, as well as RSL  
31 histories at 5 locations that have been previously considered in estimates of ice volume at LGM:  
32 Barbados, two sites at the Great Barrier Reef, Bonaparte Gulf and Sunda Shelf. We find that the  
33 difference between inferences of global mean sea level (GMSL) at LGM based on 3-D and 1-D  
34 Earth models peaks in Barbados with differences ranging from ~2.5 to 11 m, with a mean of ~6-  
35 7 m. At the other sites, the difference ranges from ~2 to -8 m, with mean differences between ~0  
36 and -3 m. After comparing different pairs of simulations, we conclude that, in general, the impact  
37 of varying the seismic model, lithospheric thickness model, background 1-D model, and scaling  
38 factor from temperature to viscosity is significant at far-field sites. Finally, while we do not find  
39 a consistent signal at the above far-field sites that would help to reconcile the LGM ice volumes  
40 estimated from GIA studies and those estimated from summing regional ice sheet

41 reconstructions, the impact is nonetheless large enough that GIA analyses of RSL records in the  
42 far field of ice sheets should include 3-D viscoelastic Earth models.

43

## 44 **1. Introduction**

45 Reconstructions of global ice volume at the Last Glacial Maximum (LGM; Clark et al.,  
46 2009) are widely explored in studies of glacial isostatic adjustment (GIA) and ice age climate.  
47 Various methodologies have been adopted in such studies. One method of inferring ice volume is  
48 based on oxygen isotope variability within sedimentary cores (e.g., Waelbroeck et al., 2002).  
49 However, this approach is complicated by the confounding effects associated with temperature,  
50 local salinity and the location of the ice mass flux (Raymo et al., 2018). A second method is  
51 based on GIA modeling, whereby the ice budget is inferred from fits to regional sea-level  
52 datasets and local constraints on ice geometry (e.g., Lambeck et al., 2017; Lambeck et al., 1998)  
53 or by tuning the total ice budget to match sea-level curves from the far field of the Pleistocene  
54 ice sheets (e.g., Nakada et al., 2016; Peltier and Fairbanks, 2006). Finally, ice sheet modeling,  
55 whether combined with GIA modeling (e.g., Gomez et al., 2020; Tarasov et al., 2012) or not  
56 (e.g., Abe-Ouchi et al., 2013; Whitehouse et al., 2012) have also provided constraints on LGM  
57 ice volume. Here, we revisit the method that uses far-field relative sea-level (RSL) data with the  
58 aim to quantify a potential bias in the estimated ice volume associated with the common GIA  
59 model assumption of a spherically-symmetric Earth viscosity structure.

60 In the 1970s and 1980s, the Climate Long-range Investigation, Mapping and Prediction  
61 (CLIMAP) project provided the first global reconstruction of climate during the LGM, including  
62 a minimum and a maximum reconstruction of ice sheet volumes (Denton and Hughes,  
63 1981). The minimum ice reconstruction located ice margins near continental margins and was

64 characterized by a global ice volume of ~127 m, in units of equivalent global mean sea level  
65 (GMSL). The maximum ice reconstruction, in contrast, featured expanded marine-based ice  
66 sheets and a global ice volume of ~163 m GMSL equivalent. Although subsequent field evidence  
67 (Dyke et al., 2002; Miller et al., 2002) and GIA modeling (e.g., Yokoyama et al., 2000) have  
68 suggested ice cover that was less extensive than the maximum ice reconstruction, it has  
69 nevertheless been commonly used as a boundary condition in climate and general circulation  
70 models (Clark and Mix, 2002). (Note that global sea-level change has other contributions beyond  
71 changes in ice mass, including changes in salinity and temperature. The term barystatic sea level  
72 has recently been adopted to distinguish the contribution of ice mass flux to GMSL change from  
73 other contributions (Gregory et al., 2019); however, we will continue to use GMSL throughout  
74 this paper since it is widely adopted within the paleoclimate literature.)

75         Following CLIMAP, the Environmental Processes of the Ice-Age: Land, Oceans,  
76         Glaciers (EPILOG) program began in 1999 with the aim of developing a comprehensive  
77         reconstruction of Earth during the LGM, using updated data and methods as well as accounting  
78         for advances made since CLIMAP (Mix et al., 2001). This program inferred minimum and  
79         maximum ice volumes of ~118 m and 130-135 m GMSL equivalent. The EPILOG  
80         reconstructions were characterized by ice sheet margins that were largely consistent with the  
81         CLIMAP maximum ice reconstruction but with a significantly different distribution of ice  
82         thickness (Clark and Mix, 2002).

83         In terms of GIA-based estimates of ice volumes, Peltier and colleagues have iteratively  
84         revised a global ice model history, publishing the ICE-6G model in 2015 (Peltier et al., 2015)  
85         and more recently, the ICE-7G model (Roy and Peltier, 2017). Differences between the two are  
86         relatively minor, with an identical ice-loading history for all regions outside of North America.

87 Our study adopts the more widely used ICE-6G model. The detailed space-time variation in the  
88 ICE-6G model is constrained using a variety of near field data, including ice margin  
89 chronologies, RSL records, and GPS measurements of crustal motion and gravity observations  
90 associated with the Gravity Recovery and Climate Experiment (GRACE). The total excess ice  
91 volume (volume of ice in excess of present-day ice volume) at LGM was tuned to fit the coral-  
92 inferred RSL record at Barbados. In this regard, LGM in the model occurs at ~26 ka with an  
93 excess ice volume of ~127 m GMSL equivalent, where ~14 m of that total resides in Antarctica.  
94 This GIA-based inference is coupled to the assumed viscoelastic Earth structure, and, in  
95 particular, the one-dimensional VM5a viscosity profile, which represents a multilayer fit to the  
96 VM2 viscosity model used in developing the earlier ICE-5G ice history (Peltier, 2004). The  
97 VM5a model involves a moderate increase in viscosity with depth, increasing from  $5 \times 10^{20}$  Pa s  
98 in the upper mantle to  $3 \times 10^{21}$  Pa s in the deep mantle.

99 Lambeck et al. (2014) used an extensive set of ~1000 RSL sediment and coral records  
100 from various locations in the far field of ice sheets to constrain the time history of integrated ice  
101 volume from 35 ka to present day using GIA modeling. Their preferred “high viscosity” Earth  
102 model yielded peak excess ice mass during LGM (21 ka) of ~134 m equivalent GMSL, with an  
103 Antarctic component of ~23 m, inferred from the difference between total ice volume and the  
104 sum of Northern Hemisphere ice volumes and mountain glaciers. Their “low viscosity” solution  
105 suggested an excess ice mass at LGM ~7 m equivalent GMSL more than the preferred “high  
106 viscosity” solution, with an excess Antarctic ice mass of ~30 m. Following Lambeck et al.  
107 (2014), Yokoyama et al. (2018) used well-dated fossil corals and coralline algae assemblages  
108 collected from the Great Barrier Reef to infer GMSL changes. Their study found an LGM low

109 stand of 125-130 m equivalent GMSL that occurred at ~20.5 ka. As in Peltier et al. (2015), both  
110 studies adopted 1-D viscosity profiles in their GIA modeling.

111         The above GIA-based estimates suggest global ice volumes during the LGM in the range  
112 of ~125-135 m equivalent GMSL with an excess Antarctic ice mass component of 14 to 30 m.  
113 While the majority of the latter range cannot be excluded when limitations associated with data  
114 and model uncertainty as well as the completeness of the observational record are considered  
115 (Briggs et al., 2014; Lecavalier and Tarasov, 2021), a growing number of ice sheet and climate  
116 modeling studies constrain this value to be less than ~10 m (e.g., Golledge et al., 2013; Ivins et  
117 al., 2013; Whitehouse et al., 2012). Gomez et al. (2013) also favor these lower estimates based  
118 on results from coupled ice sheet-sea level modeling experiments. If GIA studies of far-field  
119 RSL histories require a total excess ice volume of 125-135 m, and the Antarctic component  
120 likely does not exceed ~10 m, the question arises as to where these studies can increase ice mass  
121 flux outside Antarctica to compensate for the latter bound. This issue, which is also evident in  
122 post-LGM ice volume reconstructions (e.g., Cuzzone et al., 2016), has come to be known as the  
123 “missing ice” problem (Austermann et al., 2013; Clark and Tarasov, 2014; Simms et al., 2019).  
124 A recent ice sheet reconstruction developed using near-field ice extent and sea-level data  
125 (Gowan et al., 2021) contains an LGM ice volume of 116 m equivalent GMSL and is reported to  
126 match observed LGM RSL lowstands.

127         While the detailed methodologies used to estimate global ice volume at LGM based on  
128 far-field RSL records differ, they all involve a correction or estimate of the geographically  
129 variable signal of the GIA process. As a consequence, these studies are sensitive to model  
130 uncertainties of two types (Briggs and Tarasov, 2013; Melini and Spada, 2019): (1) those  
131 associated with limited knowledge of model inputs, such as the spatio-temporal history of ice

132 mass changes and viscoelastic Earth structure (so-called “parametric uncertainty”); and (2) those  
133 associated with inaccuracy of the forward model related to, for example, missing or poorly  
134 represented physical processes or simplifications in model set up (so-called “structural  
135 uncertainty”). A growing number of studies have sought to quantify GIA model uncertainty  
136 associated with one or both of these aspects using different approaches (e.g., Caron et al., 2018;  
137 Love et al., 2016; Simon and Riva, 2020).

138 Common simplifications of GIA models that could lead to significant structural error in  
139 some regions include: (1) the assumption of a Maxwell rheology and thus neglect of non-linear  
140 deformation and transient signals in the Earth response (e.g., Ivins et al., 2022; Kang et al., 2022;  
141 Lau et al., 2021; Ranalli, 2001; van der Wal et al., 2013; Wu and Wang, 2008), and (2) the  
142 application of spherically-symmetric Earth models and thus neglect of lateral variations in Earth  
143 structure, including elastic lithospheric thickness and mantle viscosity (e.g., Li et al., 2018;  
144 Paulson et al., 2007; van der Wal et al., 2013). Most efforts to examine and quantify this second  
145 simplification as a source of structural uncertainty have focused on near-field regions (e.g., Li et  
146 al., 2020; van der Wal et al., 2013). Austermann et al. (2013) presented the first attempt to  
147 explore this issue at a far-field location. Their study demonstrated that lateral variations in  
148 mantle viscosity in the vicinity of Barbados, in particular the presence of a high viscosity slab  
149 associated with the subduction of the Caribbean Plate, would suppress post-LGM crustal  
150 subsidence (and thus sea-level rise) associated with ocean loading in the region. They concluded  
151 that the total excess ice volume at LGM must be increased by  $\sim 7$  m equivalent GMSL relative to  
152 inferences based on standard 1-D Earth modeling to maintain a fit to the coral record of RSL  
153 change at Barbados – a requirement that accentuates the “missing ice” problem. More generally,

154 their results highlight that failing to include lateral variations in Earth structure can lead to a  
155 significant bias in estimates of LGM ice volume based on GIA modeling.

156 In the present study, we extend the analysis of Austermann et al. (2013) to consider a  
157 much wider range of 3-D GIA simulations and assess the impact of this added model complexity  
158 and realism across the entire far field of ancient ice cover. In addition to global maps of this  
159 impact, we also present results at far-field sites that have been a particular focus of previous GIA  
160 modeling of the LGM sea level low stand, including the Great Barrier Reef, Bonaparte Gulf,  
161 Sunda Shelf, and Barbados.

## 162 **2. Methods**

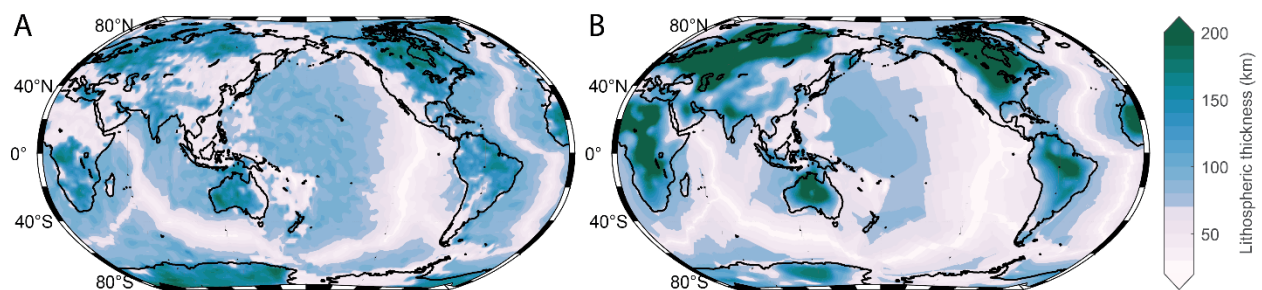
163 We present model output from a total of 40 simulations that include different realizations  
164 of 3-D Earth structure, along with predictions based on three 1-D Earth viscosity models for  
165 comparison. These simulations allow us to explore the influence of specific parameter choices on  
166 quantifying lateral variations in Earth viscosity structure and to assess the sensitivity of our GIA  
167 predictions to ice history and specific features of the 3-D Earth models, including lithospheric  
168 thickness, the globally averaged “background” 1-D viscosity model, and the magnitude and  
169 spatial variation (from different seismic models) of lateral variations in mantle viscosity. A  
170 summary of the primary model inputs varied in this study is provided in Table 1.

171 We use two global ice histories to generate simulations of RSL: ICE-6G (Peltier et al.,  
172 2015) and a model we label as ANU (Lambeck et al., 2014). The 1-D Earth models used in this  
173 study are those that are typically associated with these ice histories. In the case of ICE-6G, we  
174 adopt a version of the VM2 viscosity profile (Peltier, 2004). This version has a 3-layer viscosity  
175 profile, where the upper mantle viscosity is  $4 \times 10^{20}$  Pa s, the top ~1100 km of the lower mantle

176 has a viscosity of  $2.2 \times 10^{21}$  Pa s, and the remainder of the lower mantle has a viscosity of  $3.3 \times$   
177  $10^{21}$  Pa s. ICE-6G is generally paired with the VM5 viscosity model (Peltier et al., 2015), but the  
178 3-layer approximation of VM2 used here is very similar in both viscosity amplitudes and depth  
179 parametrization. Thus, the impact of this choice of viscosity model on our study is minor. Two  
180 classes of Earth models are favored in the adoption of the ANU ice history. In the first, the  
181 increase in viscosity from upper to lower mantle is greater than two orders of magnitude and in  
182 the second, this increase is approximately one order of magnitude (Lambeck et al., 2014). We  
183 sample both classes using a lithospheric thickness of 71 km, and upper and lower mantle pairings  
184 for both the preferred model of Lambeck et al. (2014), ( $2 \times 10^{20}$  Pa s,  $3 \times 10^{22}$  Pa s), and their  
185 second solution, ( $3 \times 10^{20}$  Pa s,  $2 \times 10^{21}$  Pa s). We label these models M1D<sub>A</sub> and M1D<sub>B</sub>,  
186 respectively. We note that, while our chosen values do not correspond to the optimal values  
187 found in Lambeck et al. (2014), they do lie within the identified 1- $\sigma$  uncertainty ranges. For  
188 example, we chose a lower mantle viscosity of  $3 \times 10^{22}$  Pas rather than  $7 \times 10^{22}$  Pas for M1D<sub>A</sub>  
189 based on the growing number of studies that suggest the smaller value is more accurate when  
190 additional datasets are considered (e.g., Hill et al., 2019; Lau et al., 2016; Nakada et al., 2015).  
191 The 3-D Earth viscosity models that we consider in this study adopt, in a spherically averaged  
192 sense, one of the three 1-D models described above.

193         Lithospheric thickness variations are adopted from two published models: Afonso et al.  
194 (2019) and Yousefi et al. (2021). The former is based on the inversion of geophysical and  
195 geochemical data to infer various properties of the lithosphere and upper mantle, including  
196 temperature. In this model, the lithospheric thickness is defined thermally by specifying the base  
197 of the lithosphere as coinciding with a given isotherm within the upper mantle model. We label  
198 this model AF. In the second model (Yousefi et al., 2021), which we label YO, lithospheric

199 (elastic) thickness in continental regions is taken from previously published models of  
200 lithospheric (elastic) thickness based on the spatial coherence of gravity and elevation data  
201 (Audet and Burgmann, 2011; Chen et al., 2017; Steffen et al., 2018). In ocean areas, it is defined  
202 thermally using sea-floor age to determine the local geotherm and assigning a given isotherm to  
203 define the base of the lithosphere. Further details on these two models can be found in the cited  
204 publications. In our analysis, these models are scaled to give the global mean of the adopted  
205 ‘background’ 1-D model (i.e., 71 km when using ANU ice history, or 96 km when using ICE-  
206 6G). Fig.1 shows both models in the case where they have been scaled so that their global  
207 average matches the lithospheric thickness of the 1-D ANU model (71 km). In AF and YO, the  
208 minimum lithospheric thickness is ~15 km and ~25 km (when scaled such that the global average  
209 is 71 km), respectively, and tends to occur near mid-ocean ridges. Maximum thicknesses,  
210 reaching ~200-350 km, are typically found in cold cratonic areas of continents. Such large values  
211 are partly a result of scaling the laterally variable lithosphere models to give a global average  
212 thickness that is equivalent to a given 1-D reference viscosity model. Some areas have large  
213 spatial gradients but are mainly found in continental regions, such as western to central North  
214 America. The AF model tends to have more smaller scale structure when compared to the YO  
215 model.



216  
217 **Figure 1:** Lithospheric thickness models used in this study, scaled to have an average thickness  
218 of 71 km. (A) AF by Afonso et al. (2019) and (B) YO by Yousefi et al. (2021).

219 We determined four models of lateral variation in mantle viscosity using published global  
 220 seismic tomographic models (Auer et al., 2014; French and Romanowicz, 2014; Ritsema et al.,  
 221 2011; Schaeffer and Lebedev, 2013). Milne et al. (2018) described and compared these four  
 222 global seismic velocity models. These models of lateral variations in viscosity are superimposed  
 223 on the three 1-D models described earlier. Our mapping from seismic wave speed anomalies to  
 224 viscosity can be described by the following three equations (Latychev et al., 2005):

$$225 \quad \delta \ln \rho(r, \theta, \phi) = \frac{\partial \ln \rho}{\partial \ln v_s}(r) \delta \ln v_s(r, \theta, \phi) \quad (1)$$

$$226 \quad \delta T(r, \theta, \phi) = -\frac{1}{\alpha(r)} \delta \ln \rho(r, \theta, \phi) \quad (2)$$

$$227 \quad \eta(r, \theta, \phi) = \eta_0(r) e^{-\epsilon \delta T(r, \theta, \phi)} \quad (3)$$

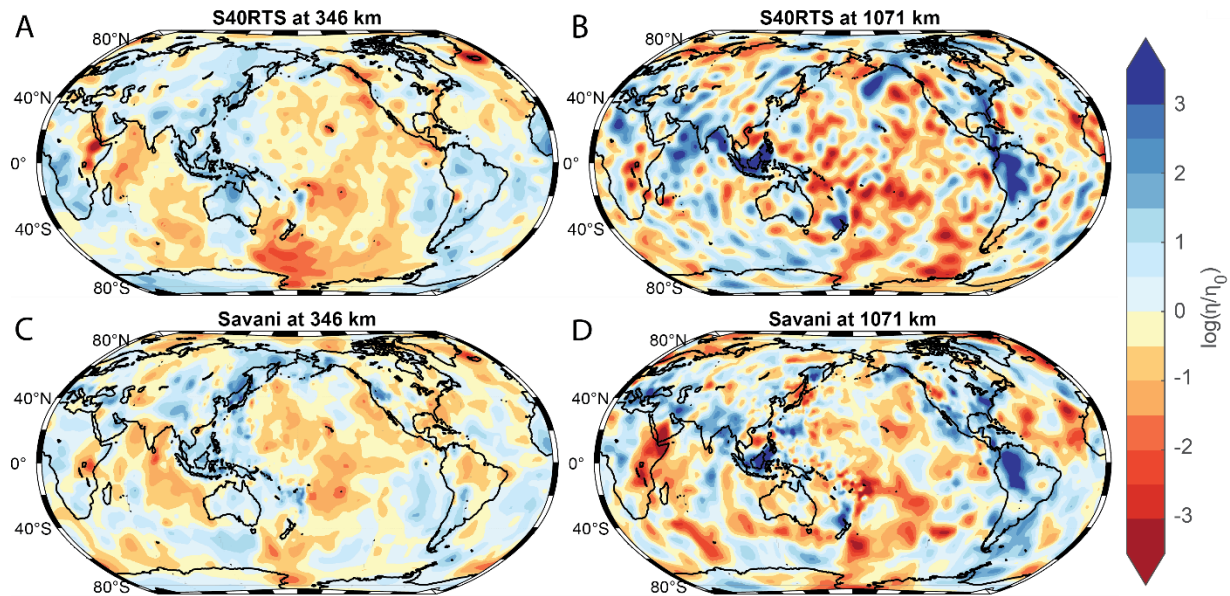
228 where  $r$ ,  $\theta$ , and  $\phi$  are the radius, colatitude, and east-longitude, and  $v_s$ ,  $\rho$ ,  $T$ , and  $\eta$  are seismic  
 229 wave speed, density, temperature, and viscosity. The parameter  $\alpha$  is the depth-dependent  
 230 coefficient of thermal expansion, and  $\frac{\partial \ln \rho}{\partial \ln v_s}$  is a depth-dependent scaling between seismic velocity  
 231 anomaly and density. The conversion from seismic wave speed to temperature and viscosity  
 232 involves a number of assumptions and the use of parameters that are poorly known. A detailed  
 233 discussion of this topic can be found in Ivins et al. (2021; Section 2.4). The parameters used here  
 234 are the same as those adopted in Austermann et al. (2013). The parameter  $\epsilon$  in equation (3)  
 235 governs the strength of the exponential dependence of viscosity on temperature, and thus the  
 236 peak-to-peak lateral variability of the former for a given input velocity model. In this study, we  
 237 consider two scaling factors: 0.04 and 0.02 °C<sup>-1</sup>. Decreasing the scaling factor from 0.04 to 0.02

238  $^{\circ}\text{C}^{-1}$  decreases the order of magnitude of the calculated range in lateral viscosity variation by  
239 approximately a factor of two over some depth extent in the mantle.

240 Viscosity variations at two depths, 346 km and 1071 km, based on the S40RTS (Ritsema  
241 et al., 2011) and Savani (Auer et al., 2014) seismic tomography models and a scaling factor of  
242  $0.04\text{ }^{\circ}\text{C}^{-1}$  are shown in Fig. 2. At 346 km, S40RTS and Savani both have viscosity variations that  
243 span several orders of magnitude. For most grid cells (99%), the variation at this depth is within  
244 about 4 orders of magnitude for each seismic model shown in Fig. 2 (range of roughly  $\pm 2$  orders  
245 magnitude about the 1-D reference value). The viscosity variation at 1071 km is larger than that  
246 at 346 km, with 99% of the values for S40RTS spanning about 7 orders of magnitude (-2.9 to 3.9  
247 about the 1-D reference value) and those for Savani spanning about 6.5 orders of magnitude (-3  
248 to 3.4). These ranges are relatively large compared to estimates based on mineral physics  
249 considerations (e.g., Karato, 2008) and so we consider them to represent an upper bound (for the  
250 adopted seismic model). The regions of high viscosity in both models tend to be associated with  
251 areas of active subduction, such as the Malay Archipelago. There are also significant differences  
252 between the two models. For instance, there are some regions where the two models have  
253 opposite signs in viscosity variations, such as the province of Québec, eastern Canada at 346 km  
254 depth and the West Indian Ocean at 1071 km depth.

255 We calculate gravitationally self-consistent sea-level change for each ice history and  
256 Earth model pairing (ICE-6G with VM2 and the VM2-based 3-D Earth models; ANU with the  
257 two corresponding 1-D Earth models and the 3-D models based upon them). We adopt the  
258 algorithm of Kendall et al. (2005) for solving the generalized sea-level equation of Mitrovica and  
259 Milne (2003). The calculations assume a Maxwell viscoelastic Earth model and accurately  
260 account for time-varying shorelines and rotational effects on sea level. The latter is computed

261 using the rotational stability theory of Mitrovica et al. (2005) which accounts for the observed  
262 oblateness of the Earth. All computations are performed using the finite volume software  
263 described in detail by Latychev et al. (2005). The computational domain is defined by a total of  
264 ~17 million nodes with 67 radial layers and a spatial resolution of ~60 km at the base of the  
265 mantle to ~12 km at the Earth's surface. Given the large model domain and the three iterations  
266 that are required to accurately compute paleotopography (and thus shoreline position), a single  
267 model run is computationally expensive. To provide a rough measure of this expense, one  
268 simulation beginning at 36 ka takes several days using ~100 compute cores.



269  
270 **Figure 2:** Lateral viscosity variations relative to the spherically averaged background value  
271 based on the S40RTS (A and B; Ritsema et al., 2011) and Savani (C and D; Auer et al., 2014)  
272 seismic models at 346 km depth (A and C), and 1071 km depth (B and D). The results shown are  
273 based on an  $\epsilon$  value of  $0.04 \text{ }^\circ\text{C}^{-1}$  (eq. 3).

274 With an aim to reduce model run time, we ran some tests to determine how sensitive  
275 predictions of LGM RSL are to the timing of model initiation. A major increase in global ice  
276 volume prior to the LGM occurs after ~36 ka in each of the chosen ice models. Therefore, this  
277 age represents a possible minimum (latest) initiation time that would accurately capture LGM

278 sea level, and this is the initiation time used in all simulations presented in this study. To test the  
279 accuracy of neglecting pre-36 ka loading changes, we performed two additional simulations (one  
280 3-D and one 1-D) which began at 80 ka. Predictions of the impact of lateral viscosity variations  
281 on RSL at LGM for simulations that differ only on the start time (Fig. S1) indicate that adopting  
282 the shorter duration introduces small, order 0.1 m, errors at far-field sites.

283 Accounting for both ice histories, the three associated background 1-D Earth models, the  
284 two models of variations in lithospheric thickness, the four seismic models, and the two  
285 temperature-to-viscosity scaling factors, there is a total of 40 simulations (24 using the ANU ice  
286 history, and 16 using ICE-6G) that include lateral variations in Earth structure (Table 2). Note  
287 that for the MID<sub>B</sub> viscosity model considered with the ANU ice model, only one  $\epsilon$  value was  
288 considered ( $0.04 \text{ }^\circ\text{C}^{-1}$ ). We also consider three simulations in which we do not include lateral  
289 variations in Earth structure (one for each of the background 1-D models associated with the two  
290 ice histories) to isolate the importance of lateral structure on LGM ice volume by considering the  
291 difference between the 3-D and 1-D simulations.

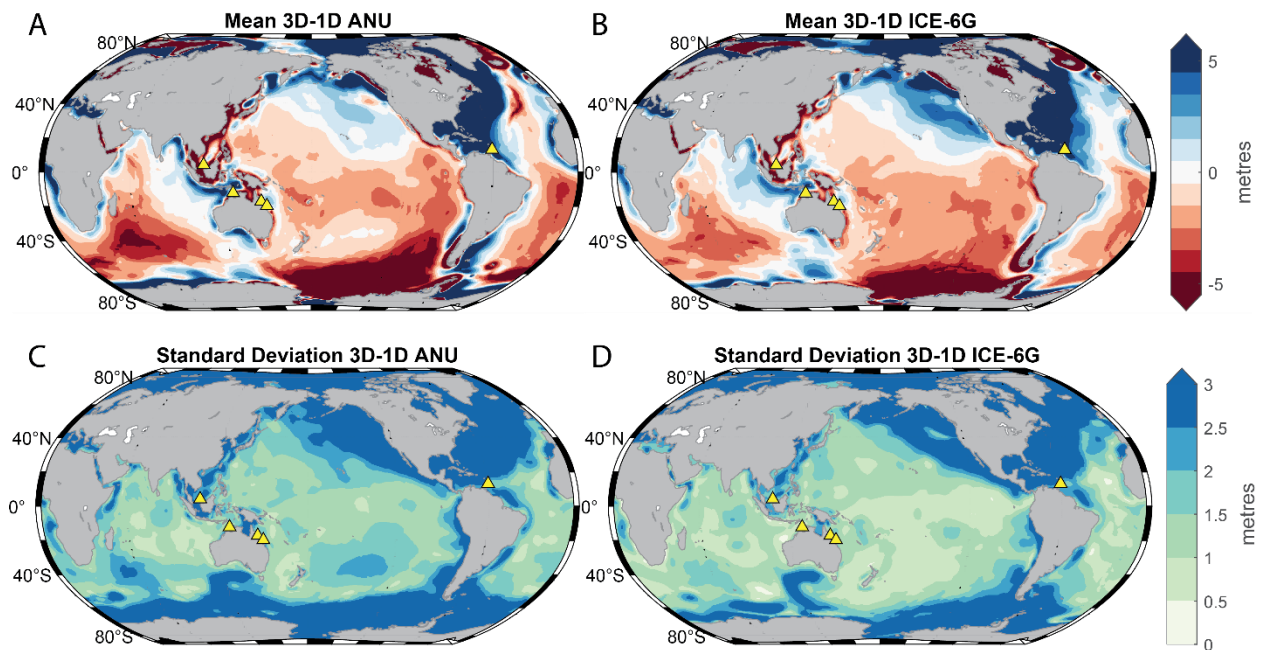
## 292 **3. Results and Discussion**

### 293 *3.1 Spatial patterns and amplitudes*

294 We computed the difference between predictions of RSL at LGM (26 ka for the ICE-6G  
295 ice history and 21 ka for the ANU ice history, i.e., when global ice volume is maximum for each  
296 ice model) based on each of the 3-D simulations in Table 2 and those based on the associated  
297 background 1-D model. Global maps of the mean and standard deviation of these runs,  
298 partitioned between the two ice histories, are shown in Fig. 3. The results for these two loading  
299 cases are qualitatively similar at low latitudes indicating that the impact of lateral variations in

300 viscosity on predictions of far-field RSL at LGM is relatively insensitive to details of the ice  
 301 history. At locations where the mean of 3D-1D model output is positive (blue in Fig. 3A-B),  
 302 such as Barbados, the sea-level prediction based on a 3-D Earth model is shallower (RSL is less  
 303 negative) than the 1-D case, and therefore has a smaller post-LGM sea-level change. Thus, if  
 304 LGM ice volume was to be inferred from one of these locations, the use of model calculations  
 305 made with a 1-D Earth model would result in an underestimate (since less global ice melt is  
 306 required to match the observed RSL rise). In contrast, at locations where the mean 3D-1D model  
 307 difference is negative, such as Noggin Pass, ice volume inferences made from the 1-D GIA  
 308 calculation would lead to an overestimate. Finally, the mean effect of lateral Earth structure is  
 309 relatively small at locations near the white band, such as Hawai'i.

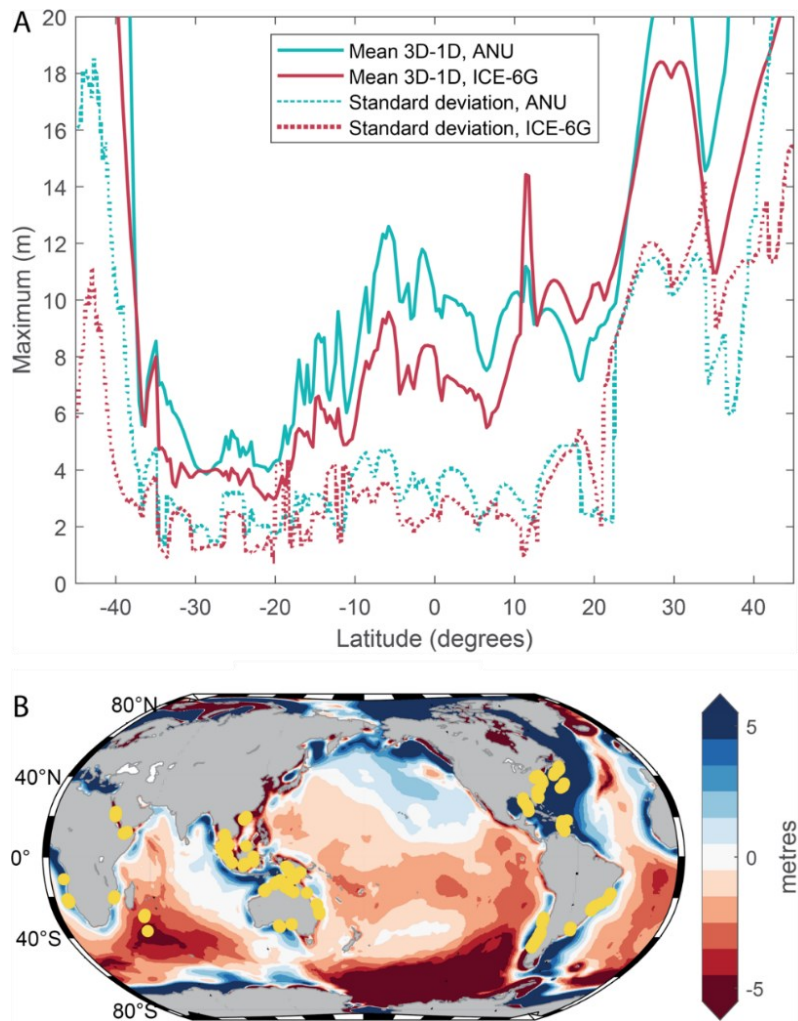
310



311

312 **Figure 3:** Mean (A, B) and standard deviation (C, D) of the difference between predictions of  
 313 RSL at LGM computed with the 3-D Earth model and the associated 1-D spherical average  
 314 (background) Earth model. (A, C) include simulations based on the ANU ice history, and (B, D)  
 315 are simulations using ICE-6G. Yellow triangles show the locations of sites in Figure 5.

316           The similarity between the two sets of results with distinct ice histories is reinforced in  
317 Fig. 4A, where we show the peak magnitude of Fig. 3A and 3B as a function of latitude (solid  
318 lines) as well as the standard deviation computed at the site at which the peak magnitude occurs  
319 (dashed lines). The location of each site is shown in Fig. 4B. These magnitudes increase rapidly  
320 as one considers latitudes that sample the peripheral bulge of the Laurentide Ice Sheet (above  
321  $\sim 20^\circ\text{N}$ ) and the West Antarctic Ice Sheet (below  $\sim 35^\circ\text{S}$ ), reaching a few 10s of m. In the former  
322 region, these large amplitudes are likely due to the larger lithospheric thickness values and  
323 higher than average viscosity in the shallow upper mantle over North America and the western  
324 North Atlantic Ocean. These two characteristics would suppress the signal of the peripheral  
325 bulge in the western North Atlantic Ocean, leading to a smaller post-LGM RSL rise. The  
326 southern Pacific Ocean has a thin oceanic lithosphere and viscosities in West Antarctica are  
327 lower than average, leading to enhanced deformation and a larger post-LGM rise for the 3-D  
328 case in this region.



329  
 330 **Figure 4:** (A) Maximum magnitude of the mean RSL difference shown in Figs. 3A and 3B as a  
 331 function of latitude (45°S to 45°N) based on the ANU (solid turquoise line) and ICE-6G (solid  
 332 red line) ice histories. For every latitude in the degree 512 Gauss-Legendre grid, we find the  
 333 maximum difference and the longitude at which it occurs. The dashed lines of associated color  
 334 show the standard deviation of the simulations at the site of maximum magnitude. (B) Same as  
 335 Fig. 3A but with yellow dots plotted at every latitude in the grid from 45°S and 45°N to show the  
 336 location of the site of maximum magnitude at that latitude.

337         Between ~20°N and ~35°S, the peak magnitude of the mean difference between the 3-D  
 338 and 1-D results varies between ~4 m and ~12 m, with a trend toward higher values moving  
 339 northward. At very low latitudes, i.e., between ±20°N, the sites showing the largest difference  
 340 between the 3-D and 1-D simulations tend to be clustered in Southeast Asia and the Caribbean,  
 341 close to local subduction zones, as well as the northern margin of Australia and in the Red Sea.

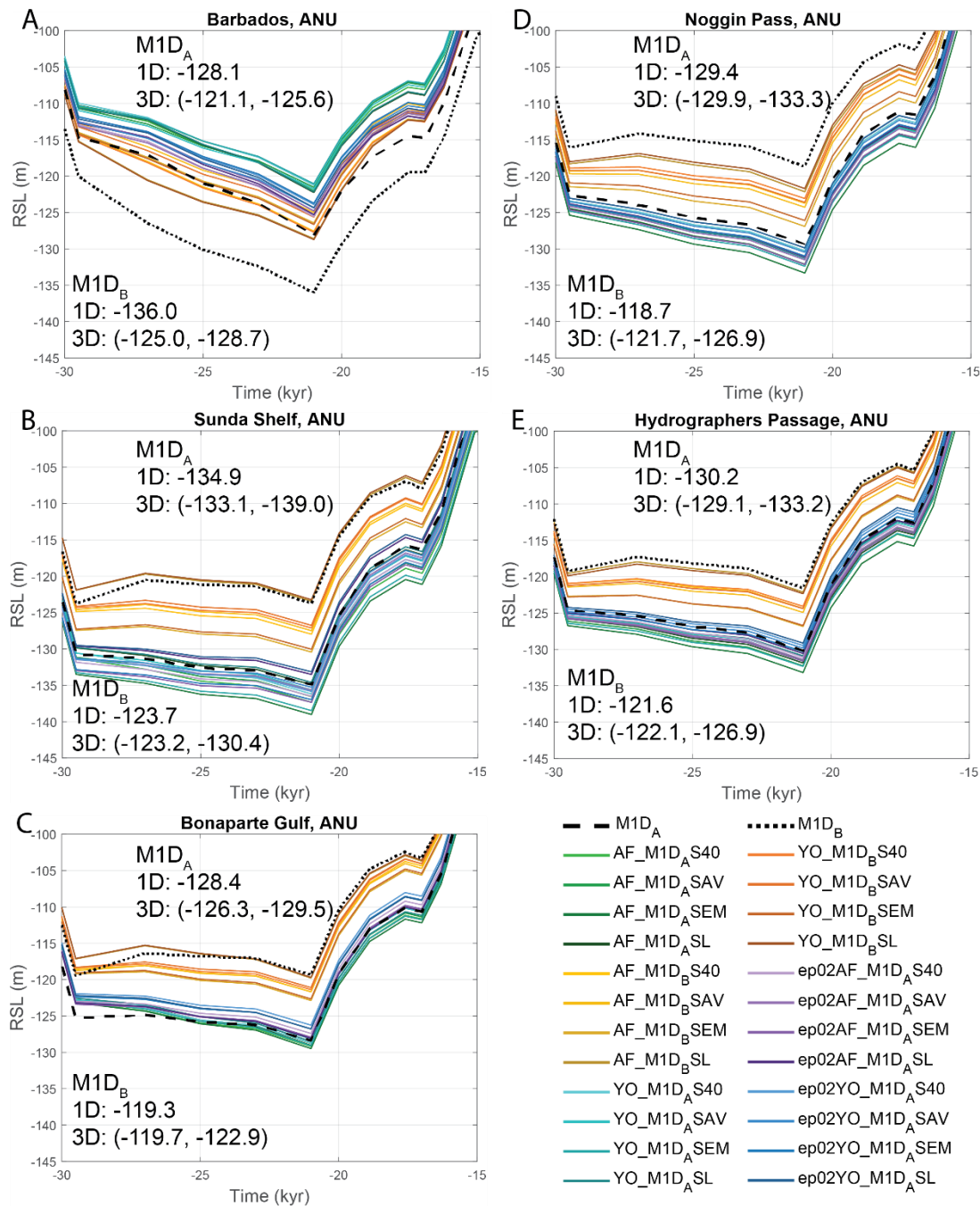
342 There is also a large difference in the Indian ocean, which is likely associated with the Central  
343 Indian Ocean Triple Junction. The lithosphere around the triple junction is thin, leading to a  
344 larger ocean-loading signal and thus a larger post-LGM RSL rise. Finally, the standard deviation  
345 ranges from ~1-4 m at the locations of peak mean difference; it is highly correlated with the  
346 signal amplitude and is significant, reaching ~30-50% of the signal.

### 347 *3.2 Far-field sites*

348 We next consider the LGM RSL predictions for the individual simulations (relative to the  
349 associated 1-D case) at 5 far-field sites with published RSL data from the LGM: Barbados,  
350 Sunda Shelf, Bonaparte Gulf, Noggin Pass, and Hydrographer's Passage (Table 3). One way to  
351 estimate the effect of the inclusion of lateral variations in Earth structure on inferences of LGM  
352 ice volume from RSL data is to look at the average effect over all simulations and all 5 sites. The  
353 mean difference between 3-D and 1-D simulations is ~0.03 m, with a standard deviation of ~3.9  
354 m. The median gives a similar result of approximately -0.9 m, and thus the average effect of  
355 lateral structure on LGM sea-level predictions is close to 0. However, as the effect of including  
356 lateral Earth structure on sea-level predictions is geographically variable (Figs 3 & 4), it is  
357 informative to consider model results at individual sites. Even at a single site, there can be a  
358 large degree of variability across simulations. For example, the difference between 3-D and 1-D  
359 simulations spans ~8.5 m at Sunda Shelf and ~7.5 m at Noggin Pass. This large variability  
360 reflects the uncertainty in defining the 3-D viscosity structure. At Noggin Pass, for instance, one  
361 of the 3-D simulations (ep02YO\_M1D<sub>ASL</sub>, Table 2) suggests that the incorporation of lateral  
362 viscosity structure would change the estimate of LGM ice volume by ~0.5 m when compared to  
363 the reference 1-D simulation. A different simulation (AF\_M1D<sub>BSEM</sub>, Table 2) suggests that the  
364 LGM ice volume estimate could be over 8 m less than the 1-D inference. Furthermore, if one

365 were to consider a single 3-D simulation at Barbados, the conclusion could be that estimates of  
366 LGM ice volume should be increased by nearly 11 m (e.g., AF\_M1D<sub>B</sub>SAV, Table 2). This  
367 highlights the importance of considering data from multiple sites as well as estimating the  
368 uncertainty related to assigning 3-D viscosity structure.

369 We can also consider Table 3 in conjunction with Fig. 5, which shows the time series of  
370 sea-level change computed with the ANU ice history at the same 5 far-field sites. The magnitude  
371 of the difference between 3-D and 1-D simulations at the LGM using the ANU ice model varies  
372 from site to site and ranges from ~0 to nearly 11 m (Fig. 5; Table 3). Analogous results based on  
373 the ICE-6G ice history are shown in Fig. S2. The range of variability in the 3-D simulations is  
374 comparable to the range in the 1-D simulations, at least at the 5 sites considered here. The site  
375 where the impact of lateral variations in mantle viscosity is largest is Barbados, with a mean  
376 difference (3-D minus 1-D) of 5.0 m, 8.9 m and 6.9 m, and a standard deviation of 1.7 m, 1.3 m,  
377 and 2.3 m for 3-D simulations adopting the 1-D background models of M1D<sub>A</sub>, M1D<sub>B</sub> and VM2,  
378 respectively. The average difference in LGM RSL between 3-D and 1-D predictions of all the  
379 simulations at Barbados is 6.5 m with a total standard deviation of 2.4 m, so the signal is large  
380 and the associated uncertainty is comparatively small. The magnitude and sign of these values  
381 are consistent with the 3-D GIA simulations of Austermann et al. (2013), who found that lateral  
382 structure perturbed the 1-D prediction by ~7 m. Note that in all simulations, the 3-D prediction of  
383 RSL at LGM at Barbados is shallower (i.e., there is a smaller post-LGM sea-level rise) than the  
384 associated 1-D prediction, indicating that the interpretation described by Austermann et al.  
385 (2013) – an ocean-loading induced reduction of crustal subsidence due to the high viscosity slab  
386 beneath the site and/or a change in the dynamics of the peripheral bulge – are universal features  
387 of the 3-D model runs presented here.



388

389 **Figure 5:** Relative sea-level curves predicted for all simulations adopting the ANU ice history  
390 (Lambeck et al., 2014) from 30 ka to 15 ka at (A) Barbados, (B) Sunda Shelf, (C) Bonaparte  
391 Gulf, (D) Noggin Pass, Great Barrier Reef, and (E) Hydrographer's Passage, Great Barrier Reef.  
392 Site locations are shown as yellow triangles in Figure 3. Inset labels specify the full range of  
393 predicted RSL at LGM for the 3-D models and the associated 1-D spherically averaged  
394 background model. As discussed in the text, we adopt two different background 1-D models,  
395 M1D<sub>A</sub> and M1D<sub>B</sub>, for the ANU ice history.

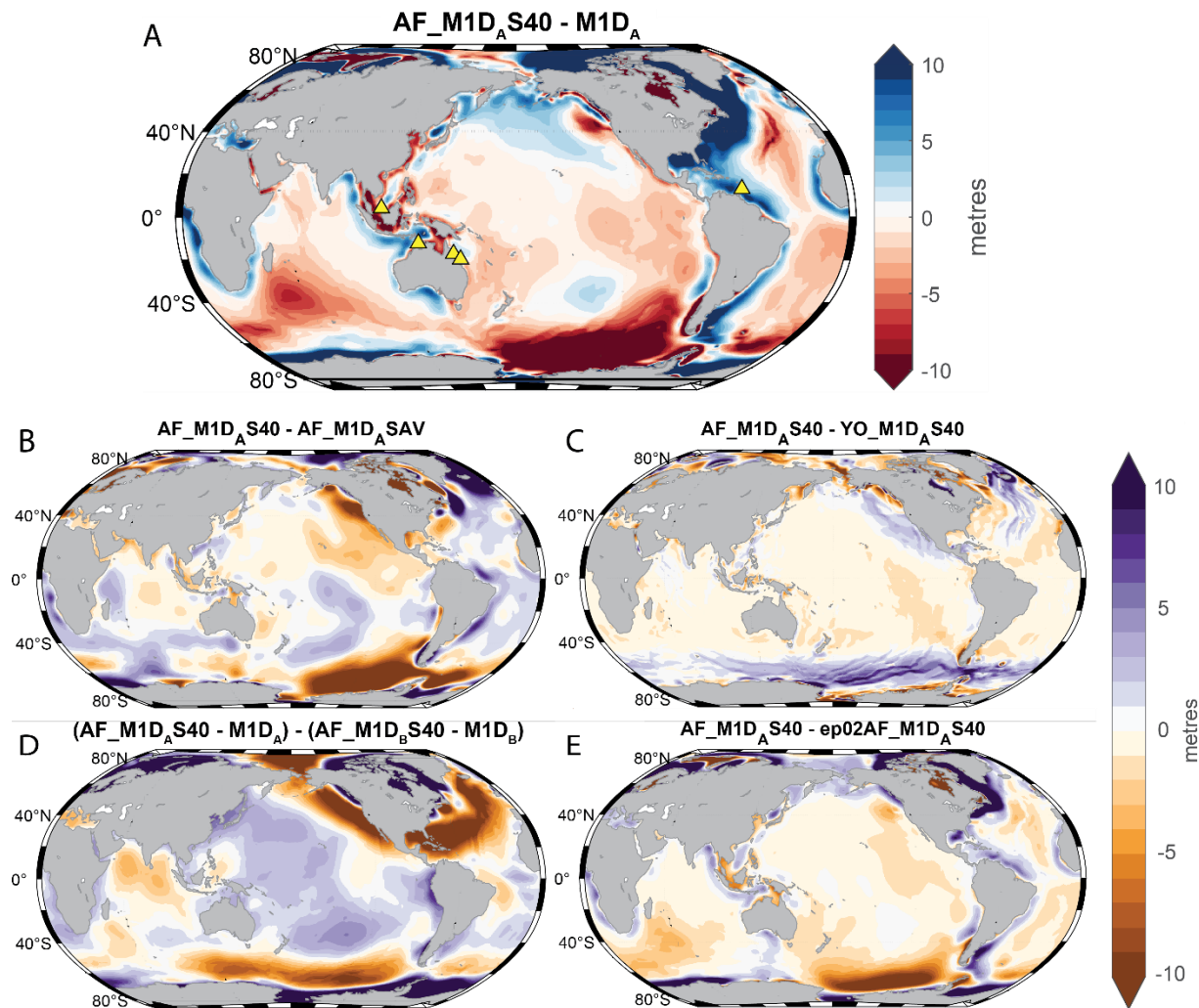
396 At the Noggin Pass site, offshore of Australia and on the Great Barrier Reef, introducing  
397 lateral variations in Earth viscosity structure also perturbs predictions of RSL at LGM in a  
398 consistent manner, with an average signal amplitude that exceeds the standard deviation.  
399 However, in contrast to Barbados, the effect is to deepen the LGM low stand by 0.5-8.2 m (with  
400 a mean of  $\sim -2.9$  an associated standard deviation of 1.8 m), which, if used to infer LGM ice  
401 volume, would lead to a lower estimate than that based on a 1-D model. At this site, the 3-D  
402 Earth models are characterized by a significantly thinner lithosphere ( $\sim 38$  km in AF and  $\sim 56$  km  
403 in YO) than the associated 1-D model used as a background state (Fig. 1) and thus ocean loading  
404 post-LGM would drive a larger offshore crustal subsidence (and sea-level rise) associated with  
405 so-called “continental levering” (Clark et al., 1978; Nakada and Lambeck, 1989). A similar  
406 interpretation could apply for Hydrographer’s Passage on the Great Barrier Reef, although a  
407 small number of 3-D simulations do predict a shallowing of the low stand relative to the 1-D  
408 case.

409 At Sunda Shelf, the mean difference between 3-D and 1-D simulations is -1.9 m, with a  
410 standard deviation of similar magnitude (2.1 m). While the estimated model uncertainty is of a  
411 similar size as the signal, most of the simulations show a deepening of the LGM low stand,  
412 suggesting that lateral Earth structure is contributing to a consistent offset. Lambeck et al. (2002)  
413 have shown that there is a large ocean loading signal at Sunda Shelf, which is likely affected by  
414 lateral variations in Earth structure. Fig. 1 shows that the lithosphere is thinner than average (71  
415 km),  $\sim 40$ -45 km in both 3-D models of lithospheric thickness at this location, which may lead to  
416 an amplification of the ocean loading signal. We also note that the largest signals at Sunda Shelf  
417 tend to occur with the model we labeled SEM (French and Romanowicz, 2014). Fig. S3 shows  
418 viscosity variations in the SEM model at 346 km and 1071 km depth. Beneath the Sunda Shelf,

419 the SEM model is  $\sim 1$  order of magnitude less viscous than S40RTS and just under 1 order of  
420 magnitude less viscous than Savani at 346 km depth, which likely also contributes to the  
421 amplification of the ocean loading signal. Finally, at Bonaparte Gulf, the impact of lateral  
422 variations in mantle structure on RSL at LGM can be of either sign, and the mean value of the  
423 perturbation is relatively small.

### 424 *3.3 Isolating parameter sensitivities*

425 To explore the sensitivity of the results to individual aspects of the adopted 3-D Earth  
426 model, we begin with a map (Fig. 6A) showing the difference between a prediction of RSL at  
427 LGM for the run adopting the Ritsema et al. (2011) seismic tomography model S40RTS, the  
428 lithospheric thickness variations given by Afonso et al. (2019), a temperature-to-viscosity scaling  
429 factor of  $0.04 \text{ } ^\circ\text{C}^{-1}$ , a spherical average background structure M1DA, and the 1-D simulation  
430 based on M1DA. Within  $20^\circ$  of the equator, the magnitude peaks at  $\sim 10$  m in the area close to  
431 Barbados and the northern shoreline of South America and  $\sim 16$  m in Makassar Strait just east of  
432 Borneo. As we noted above, the largest signals are evident close to subduction zones, where high  
433 viscosity subducted slabs impact solid Earth deformation, and on continental margins, where the  
434 continental levering signal can be strongly affected by variations in lithospheric thickness (and  
435 asthenospheric viscosity).



436

437 **Figure 6:** (A) Difference in RSL (3D minus 1D) at LGM predicted using the ANU ice history  
 438 (Lambeck et al., 2014) with a 3-D Earth model based on the seismic tomographic model S40RTS  
 439 of Ritsema et al. (2011), the lithospheric thickness model of Afonso et al. (2019) scaled to give a  
 440 global mean of 71 km, a temperature-to-viscosity scaling factor of  $0.04^{\circ}\text{C}^{-1}$ , and the M1D<sub>A</sub> 1-D  
 441 viscosity profile. Yellow triangles show the locations of sites in Figure 5. Results in other frames  
 442 show the differences between those in A and an identical simulation with the exception that we  
 443 adopt the (B) seismic model of Auer et al. (2014), (C) lithospheric thickness model of Yousefi et  
 444 al. (2021), (D) background 1-D model M1D<sub>B</sub>, and (E) scaling factor from temperature to  
 445 viscosity of  $0.02^{\circ}\text{C}^{-1}$ .

446

447

448

449

Next, we alter one aspect in the construction of the 3-D model, including the adopted  
 seismic tomography model, lithospheric thickness model, background 1-D model, and scaling  
 factor from temperature to viscosity (Fig. 6B-E, respectively). Comparison of the model results  
 in Fig. 6B-E with 6A suggests that adopting a different lithospheric thickness model has the

450 smallest impact on predicted far-field RSL differences in most regions, albeit in simulations in  
451 which the global averages of the two lithospheric thickness models are the same. There are  
452 significant differences near some mid-ocean ridges, where the YO lithosphere model tends to  
453 give lower RSL values than AF. A change in the temperature to viscosity scaling factor ( $\epsilon$ ) also  
454 has a relatively small effect in most regions, which may reflect the relatively long wavelength of  
455 the S40RTS seismic tomography model (Ritsema et al., 2011). There is also a spatial correlation  
456 between Fig. 6A and 6E, showing that the main effect of reducing the scaling factor is to reduce  
457 the amplitude of spatial variability. The results in Table 3 are also suggestive of this correlation,  
458 as the simulations with the smaller scaling factor tend to have a smaller signal at all sites  
459 considered. This reflects the effect of reducing the scaling factor from temperature to viscosity  
460 on the Earth structure, where a smaller scaling factor leads to smaller peak-to-peak variability.  
461 The largest impact on the predictions occurs with a change in the choice of seismic model, which  
462 alters the geometry of the lateral variations in mantle viscosity, and the spherically averaged (1-  
463 D) background model. Regarding the former, as mentioned above, both the amplitude and sign  
464 of lateral variations in viscosity differ across different seismic models, which explains the large  
465 effect of the choice of seismic model on predicted LGM RSL. Plotting the maximum amplitude  
466 of the RSL fields in Fig. 6 (B-E) as a function of latitude shows that all four of these model  
467 aspects can contribute significantly at some far-field locations (Fig. S4).

#### 468 **4. Conclusions**

469 The impact of lateral variations in Earth structure on LGM sea-level predictions varies  
470 based on location. Of the five far-field sites considered in this study, the largest effect tends to  
471 occur at Barbados, with differences in predictions of RSL at LGM between the 3-D and  
472 associated 1-D simulations ranging from ~2.5 to 11 m, and a mean of 6.3 m and 6.9 m for the

473 ANU and ICE-6G runs, respectively. The mean impact of lateral variations in viscosity structure  
474 at the other 4 sites ranges from <1 m at Bonaparte Gulf to ~3 m at Noggin Pass on the Great  
475 Barrier Reef (see Table 3). Notably, the incorporation of lateral structure across all simulations  
476 has a consistent effect on predictions at Barbados, shallowing the LGM low stand, and at Noggin  
477 Pass, where the predicted low stand is deepened. The former is due to a reduction in ocean  
478 loading-induced crustal deformation associated with the high viscosity slab subducting under the  
479 Caribbean Plate and/or a change in peripheral bulge dynamics (Austermann et al., 2013). The  
480 latter may reflect an amplified continental levering signal due to the thin lithosphere local to the  
481 site in both models of global lithospheric thickness we have adopted.

482         We have considered the impact of varying several aspects that govern the estimated 3-D  
483 viscosity structure on the predictions, including the seismic tomography model, spherically  
484 averaged (1-D) background viscosity, lithospheric thickness model, and scaling factor that  
485 governs the mapping from temperature variations to viscosity. All four aspects are significant  
486 and can make a significant difference when considering their effects on sea-level predictions. If  
487 we assume that choices in these different model inputs reflect, to some extent, the uncertainty in  
488 these aspects for defining 3-D Earth structure, then we conclude that uncertainties in the seismic  
489 model and 1-D background model upon which the lateral variations are superimposed make the  
490 largest difference in most locations. We also note, as mentioned in the Introduction, that there are  
491 other sources of structural uncertainty beyond lateral variations in Earth structure that would  
492 affect GIA model output. Our simulations assume a Maxwell viscoelastic Earth, but laboratory  
493 experiments and some geodetic data at subduction zones suggest that a Maxwell rheology may  
494 not be sufficient (e.g., Ranalli, 2001). Though computationally challenging, recent studies  
495 incorporating nonlinear rheology (Kang et al., 2022) or higher order linear rheology (Ivins et al.,

496 2022) in GIA models suggest that these complexities may become important in reconciling  
497 observations.

498 Finally, in the Introduction we discussed the so-called “missing ice” problem, that is, the  
499 discrepancy between LGM ice volume estimates based on far-field RSL records versus those  
500 based on regional ice sheet reconstructions. For some 3-D models and at some sites, the effect of  
501 including lateral variations in Earth structure could help to partially address this problem.  
502 However, in all the simulations that we have considered here, there is no consistent, high  
503 magnitude signal across all models and at all far-field sites. Thus, we conclude that our analysis  
504 does not have significant implications for seeking a solution to this problem. Nevertheless, the  
505 impact of lateral variations in Earth structure on predictions of far-field RSL at LGM is both site-  
506 dependent and large enough (Fig. 3) such that LGM ice volume estimates should consider  
507 multiple sites and be based on 3-D viscoelastic Earth models.

## 508 **Acknowledgements**

509 The authors acknowledge PALSEA, a working group of the International Union for Quaternary  
510 Sciences (INQUA) and Past Global Changes (PAGES), which in turn received support from the  
511 Swiss Academy of Sciences and the Chinese Academy of Sciences. Anthony Purcell, Erik Ivins,  
512 and an anonymous reviewer provided constructive comments that helped improve the  
513 manuscript. This material is also based upon work supported by the Fonds de Recherche du  
514 Québec–Nature et technologies [L.P.], Natural Sciences and Engineering Research Council of  
515 Canada [L.P. and G.A.M], Star-Friedman Challenge [L.P. and K.L.], Harvard University Center  
516 for the Environment summer research grant [S.L.G.], NSF grant EAR 19-03518 [J.A.], NASA  
517 grant NNX17AE17G [M.J.H. and J.X.M.], the Australian Government's *Exploring for the Future*

518 program [M.J.H.], John D. and Catherine T. MacArthur Foundation [J.X.M.], and Harvard  
519 University [L.P., K.L., M.J.H., and J.X.M.].

520

521 **Table 1:** Summary of the primary model inputs varied in this study.

Parameter	Model/Range	Reference
Lithospheric thickness	AF	Afonso et al. (2019)
	YO	Yousefi et al. (2021)
Seismic velocity	S40RTS	Ritsema et al. (2011)
	Savani	Auer et al. (2014)
	SEMUCB-WM1	French and Romanowicz (2014)
	SL2013	Schaeffer and Lebedev (2013)
Background viscosity (Pa s)	M1D <sub>A</sub> (Upper mantle: $2 \times 10^{20}$ Lower mantle: $3 \times 10^{22}$ )	Lambeck et al. (2014)
	M1D <sub>B</sub> (Upper mantle: $3 \times 10^{20}$ Lower mantle: $2 \times 10^{21}$ )	Lambeck et al. (2014)
	VM2 (Upper mantle: $4 \times 10^{20}$ Top ~1100 km of lower mantle: $2.2 \times 10^{21}$ Remainder of lower mantle: $3.3 \times 10^{21}$ )	Peltier (2004)
Temperature to viscosity scaling ( $\epsilon$ ; $^{\circ}\text{C}^{-1}$ )	0.02 or 0.04	Austermann et al. (2013)

522

523

524 **Table 2:** Specifications of each of the 40 simulations.

Name of Simulation	Ice history	Lithospheric thickness	Viscosity structure	Reference 1-D Model	Scaling factor ( $^{\circ}\text{C}^{-1}$ )
AF_M1D <sub>A</sub> S40	ANU	AF	S40RTS	M1D <sub>A</sub>	0.04
AF_M1D <sub>A</sub> SAV	ANU	AF	Savani	M1D <sub>A</sub>	0.04
AF_M1D <sub>A</sub> SEM	ANU	AF	SEMUCB-WM1	M1D <sub>A</sub>	0.04
AF_M1D <sub>A</sub> SL	ANU	AF	SL2013	M1D <sub>A</sub>	0.04
AF_M1D <sub>B</sub> S40	ANU	AF	S40RTS	M1D <sub>B</sub>	0.04
AF_M1D <sub>B</sub> SAV	ANU	AF	Savani	M1D <sub>B</sub>	0.04
AF_M1D <sub>B</sub> SEM	ANU	AF	SEMUCB-WM1	M1D <sub>B</sub>	0.04
AF_M1D <sub>B</sub> SL	ANU	AF	SL2013	M1D <sub>B</sub>	0.04
YO_M1D <sub>A</sub> S40	ANU	YO	S40RTS	M1D <sub>A</sub>	0.04
YO_M1D <sub>A</sub> SAV	ANU	YO	Savani	M1D <sub>A</sub>	0.04
YO_M1D <sub>A</sub> SEM	ANU	YO	SEMUCB-WM1	M1D <sub>A</sub>	0.04
YO_M1D <sub>A</sub> SL	ANU	YO	SL2013	M1D <sub>A</sub>	0.04
YO_M1D <sub>B</sub> S40	ANU	YO	S40RTS	M1D <sub>B</sub>	0.04
YO_M1D <sub>B</sub> SAV	ANU	YO	Savani	M1D <sub>B</sub>	0.04
YO_M1D <sub>B</sub> SEM	ANU	YO	SEMUCB-WM1	M1D <sub>B</sub>	0.04
YO_M1D <sub>B</sub> SL	ANU	YO	SL2013	M1D <sub>B</sub>	0.04
ep02AF_M1D <sub>A</sub> S40	ANU	AF	S40RTS	M1D <sub>A</sub>	0.02
ep02AF_M1D <sub>A</sub> SAV	ANU	AF	Savani	M1D <sub>A</sub>	0.02
ep02AF_M1D <sub>A</sub> SEM	ANU	AF	SEMUCB-WM1	M1D <sub>A</sub>	0.02
ep02AF_M1D <sub>A</sub> SL	ANU	AF	SL2013	M1D <sub>A</sub>	0.02
ep02YO_M1D <sub>A</sub> S40	ANU	YO	S40RTS	M1D <sub>A</sub>	0.02
ep02YO_M1D <sub>A</sub> SAV	ANU	YO	Savani	M1D <sub>A</sub>	0.02
ep02YO_M1D <sub>A</sub> SEM	ANU	YO	SEMUCB-WM1	M1D <sub>A</sub>	0.02
ep02YO_M1D <sub>A</sub> SL	ANU	YO	SL2013	M1D <sub>A</sub>	0.02
AF_96VM2_S40	ICE-6G	AF	S40RTS	96VM2	0.04
AF_96VM2_SAV	ICE-6G	AF	Savani	96VM2	0.04
AF_96VM2_SEM	ICE-6G	AF	SEMUCB-WM1	96VM2	0.04
AF_96VM2_SL	ICE-6G	AF	SL2013	96VM2	0.04
YO_96VM2_S40	ICE-6G	YO	S40RTS	96VM2	0.04
YO_96VM2_SAV	ICE-6G	YO	Savani	96VM2	0.04
YO_96VM2_SEM	ICE-6G	YO	SEMUCB-WM1	96VM2	0.04
YO_96VM2_SL	ICE-6G	YO	SL2013	96VM2	0.04
ep02AF_96VM2_S40	ICE-6G	AF	S40RTS	96VM2	0.02
ep02AF_96VM2_SAV	ICE-6G	AF	Savani	96VM2	0.02
ep02AF_96VM2_SEM	ICE-6G	AF	SEMUCB-WM1	96VM2	0.02

<b>Name of Simulation</b>	<b>Ice history</b>	<b>Lithospheric thickness</b>	<b>Viscosity structure</b>	<b>Reference 1-D Model</b>	<b>Scaling factor (°C<sup>-1</sup>)</b>
ep02AF_96VM2_SL	ICE-6G	AF	SL2013	96VM2	0.02
ep02YO_96VM2_S40	ICE-6G	YO	S40RTS	96VM2	0.02
ep02YO_96VM2_SAV	ICE-6G	YO	Savani	96VM2	0.02
ep02YO_96VM2_SEM	ICE-6G	YO	SEMUCB-WM1	96VM2	0.02
ep02YO_96VM2_SL	ICE-6G	YO	SL2013	96VM2	0.02

525

526

527

528 **Table 3:** The difference between predictions of RSL at LGM computed with the 3-D Earth  
 529 model and the associated 1-D spherically averaged (background) Earth model. The mean,  
 530 median, and standard deviation of each group of simulations (grouped by background Earth  
 531 model) are also included.

Name of Run	Barbados	Sunda Shelf	Bonaparte Gulf	Noggin Pass	Hydrographer's Passage
AF_M1D <sub>A</sub> S40	6.12	-2.39	-0.83	-1.84	-1.28
AF_M1D <sub>A</sub> SAV	6.59	-1.60	-0.39	-2.74	-2.07
AF_M1D <sub>A</sub> SEM	7.00	-4.07	-1.13	-3.96	-2.99
AF_M1D <sub>A</sub> SL	5.88	0.03	-0.68	-2.77	-1.67
YO_M1D <sub>A</sub> S40	6.89	-1.25	-0.36	-0.90	-0.16
YO_M1D <sub>A</sub> SAV	6.36	-0.68	0.18	-1.93	-0.84
YO_M1D <sub>A</sub> SEM	7.08	-3.54	-0.73	-3.03	-2.14
YO_M1D <sub>A</sub> SL	5.99	0.36	-0.16	-1.88	-0.69
ep02AF_M1D <sub>A</sub> S40	2.57	-1.55	0.94	-1.77	-0.89
ep02AF_M1D <sub>A</sub> SAV	2.82	-0.72	0.38	-2.14	-1.20
ep02AF_M1D <sub>A</sub> SEM	3.34	-2.40	0.43	-2.78	-1.42
ep02AF_M1D <sub>A</sub> SL	2.83	1.44	0.26	-1.73	-0.37
ep02YO_M1D <sub>A</sub> S40	4.21	-0.90	2.09	-0.51	0.72
ep02YO_M1D <sub>A</sub> SAV	3.76	-0.32	1.59	-1.09	0.37
ep02YO_M1D <sub>A</sub> SEM	4.40	-2.04	1.58	-1.62	-0.08
ep02YO_M1D <sub>A</sub> SL	3.79	1.80	1.56	-0.50	1.05
<b>MEAN</b>	4.98	-1.11	0.29	-1.95	-0.85
<b>MEDIAN</b>	5.14	-1.08	0.22	-1.86	-0.86
<b>STANDARD DEVIATION</b>	1.66	1.61	1.00	0.95	1.09
AF_M1D <sub>B</sub> S40	8.41	-4.27	-2.35	-5.05	-2.80
AF_M1D <sub>B</sub> SAV	10.97	-3.78	-2.36	-5.60	-3.37
AF_M1D <sub>B</sub> SEM	9.55	-6.72	-3.54	-8.23	-5.30
AF_M1D <sub>B</sub> SL	7.38	0.27	-0.46	-3.47	-0.57
YO_M1D <sub>B</sub> S40	8.27	-3.41	-2.05	-4.40	-2.51
YO_M1D <sub>B</sub> SAV	10.36	-3.05	-1.77	-4.92	-2.83
YO_M1D <sub>B</sub> SEM	9.34	-6.33	-3.33	-7.42	-5.16
YO_M1D <sub>B</sub> SL	7.26	0.48	-0.37	-3.04	-0.79
<b>MEAN</b>	8.94	-3.35	-2.03	-5.27	-2.92
<b>MEDIAN</b>	8.88	-3.60	-2.20	-4.98	-2.82
<b>STANDARD DEVIATION</b>	1.34	2.65	1.16	1.80	1.74

532

533

534 **Table 3 (continued)**

<b>Name of Run</b>	<b>Barbados</b>	<b>Sunda Shelf</b>	<b>Bonaparte Gulf</b>	<b>Noggin Pass</b>	<b>Hydrographer's Passage</b>
AF_96VM2_S40	9.65	-2.78	-0.40	-3.11	-1.97
AF_96VM2_SAV	10.52	-2.13	-0.57	-3.46	-2.42
AF_96VM2_SEM	9.20	-5.10	-1.42	-5.65	-4.20
AF_96VM2_SL	6.31	1.02	0.25	-2.30	-1.12
YO_96VM2_S40	9.83	-2.49	-0.25	-2.54	-1.19
YO_96VM2_SAV	10.25	-2.16	0.11	-2.84	-1.46
YO_96VM2_SEM	8.88	-5.48	-1.16	-4.80	-3.32
YO_96VM2_SL	6.38	0.68	0.60	-1.75	-0.09
ep02AF_96VM2_S40	4.53	-1.73	0.98	-1.83	-1.39
ep02AF_96VM2_SAV	5.74	-1.38	0.38	-1.95	-1.55
ep02AF_96VM2_SEM	5.24	-3.88	0.39	-3.22	-2.23
ep02AF_96VM2_SL	3.59	0.73	0.45	-1.66	-1.01
ep02YO_96VM2_S40	4.94	-1.62	1.76	-1.03	-0.12
ep02YO_96VM2_SAV	5.95	-1.54	1.48	-1.23	-0.21
ep02YO_96VM2_SEM	5.27	-3.93	1.14	-2.23	-0.98
ep02YO_96VM2_SL	4.02	0.56	1.43	-0.89	0.47
<b>MEAN</b>	6.89	-1.95	0.32	-2.53	-1.42
<b>MEDIAN</b>	6.13	-1.93	0.39	-2.27	-1.29
<b>STANDARD DEVIATION</b>	2.41	2.02	0.92	1.31	1.22
<b>TOTAL MEAN</b>	6.54	-1.90	-0.16	-2.85	-1.49
<b>TOTAL MEDIAN</b>	6.33	-1.67	-0.02	-2.42	-1.24
<b>TOTAL STD DEV</b>	2.42	2.12	1.36	1.78	1.47

535

536

537 **References**

- 538 Abe-Ouchi, A., Saito, F., Kawamura, K., Raymo, M.E., Okuno, J., Takahashi, K., Blatter, H.,  
539 2013. Insolation-driven 100,000-year glacial cycles and hysteresis of ice-sheet volume. *Nature*  
540 500, 190-193.
- 541 Afonso, J.C., Salajegheh, F., Szwillus, W., Ebbing, J., Gaina, C., 2019. A global reference model  
542 of the lithosphere and upper mantle from joint inversion and analysis of multiple data sets.  
543 *Geophys. J. Int.* 217, 1602-1628.
- 544 Audet, P., Burgmann, R., 2011. Dominant role of tectonic inheritance in supercontinent cycles.  
545 *Nat. Geosci.* 4, 184-187.
- 546 Auer, L., Boschi, L., Becker, T.W., Nissen-Meyer, T., Giardini, D., 2014. Savani: A variable  
547 resolution whole-mantle model of anisotropic shear velocity variations based on multiple data  
548 sets. *J. Geophys. Res. Solid Earth* 119, 3006-3034.
- 549 Austermann, J., Mitrovica, J.X., Latychev, K., Milne, G.A., 2013. Barbados-based estimate of  
550 ice volume at Last Glacial Maximum affected by subducted plate. *Nat. Geosci.* 6, 553-557.
- 551 Briggs, R.D., Pollard, D., Tarasov, L., 2014. A data-constrained large ensemble analysis of  
552 Antarctic evolution since the Eemian. *Quat. Sci. Rev.* 103, 91-115.
- 553 Briggs, R.D., Tarasov, L., 2013. How to evaluate model-derived deglaciation chronologies: a  
554 case study using Antarctica. *Quat. Sci. Rev.* 63, 109-127.
- 555 Caron, L., Ivins, E.R., Larour, E., Adhikari, S., Nilsson, J., Blewitt, G., 2018. GIA Model  
556 Statistics for GRACE Hydrology, Cryosphere, and Ocean Science. *Geophys. Res. Lett.* 45, 2203-  
557 2212.
- 558 Chen, B., Haeger, C., Kaban, M.K., Petrunin, A.G., 2017. Variations of the effective elastic  
559 thickness reveal tectonic fragmentation of the Antarctic lithosphere. *Tectonophysics* 746, 412-  
560 424.
- 561 Clark, J.A., Farrell, W.E., Peltier, W.R., 1978. Global Changes in Postglacial Sea Level: A  
562 Numerical Calculation. *Quat. Res.* 9, 265-287.
- 563 Clark, P.U., Dyke, A.S., Shakun, J.D., Carlson, A.E., Clark, J., Wohlfarth, B., Mitrovica, J.X.,  
564 Hostetler, S.W., McCabe, A.M., 2009. The Last Glacial Maximum. *Science* 325, 710-714.
- 565 Clark, P.U., Mix, A.C., 2002. Ice sheets and sea level of the Last Glacial Maximum. *Quat. Sci.*  
566 *Rev.* 21, 1-7.
- 567 Clark, P.U., Tarasov, L., 2014. Closing the sea level budget at the Last Glacial Maximum. *Proc.*  
568 *Natl. Acad. Sci. U.S.A.* 111, 15861-15862.
- 569 Cuzzone, J.K., Clark, P.U., Carlson, A.E., Ullman, D.J., Rinterknecht, V.R., Milne, G.A.,  
570 Lunkka, J.P., Wohlfarth, B., Marcott, S.A., Caffee, M., 2016. Final deglaciation of the  
571 Scandinavian Ice Sheet and implications for the Holocene global sea-level budget. *Earth Planet.*  
572 *Sci. Lett.* 448, 34-41.
- 573 Denton, G.H., Hughes, T.J., 1981. *The last great ice sheets.* Wiley.

574 Dyke, A.S., Andrews, J.T., Clark, P.U., England, J.H., Miller, G.H., Shaw, J., Veillette, J.J.,  
575 2002. The Laurentide and Innuitian ice sheets during the Last Glacial Maximum. *Quat. Sci. Rev.*  
576 21, 9-31.

577 French, S.W., Romanowicz, B.A., 2014. Whole-mantle radially anisotropic shear velocity  
578 structure from spectral-element waveform tomography. *Geophys. J. Int.* 199, 1303-1327.

579 Gollledge, N.R., Levy, R.H., McKay, R.M., Fogwill, C.J., White, D.A., Graham, A.G.C., Smith,  
580 J.A., Hillenbrand, C.D., Licht, K.J., Denton, G.H., Ackert, R.P., Maas, S.M., Hall, B.L., 2013.  
581 Glaciology and geological signature of the Last Glacial Maximum Antarctic ice sheet. *Quat. Sci.*  
582 *Rev.* 78, 225-247.

583 Gomez, N., Pollard, D., Mitrovica, J.X., 2013. A 3-D coupled ice sheet - sea level model applied  
584 to Antarctica through the last 40 ky. *Earth Planet. Sci. Lett.* 384, 88-99.

585 Gomez, N., Weber, M.E., Clark, P.U., Mitrovica, J.X., Han, H.K., 2020. Antarctic ice dynamics  
586 amplified by Northern Hemisphere sea-level forcing. *Nature* 587, 600-604.

587 Gowan, E.J., Zhang, X., Khosravi, S., Rovere, A., Stocchi, P., Hughes, A.L.C., Gyllencreutz, R.,  
588 Mangerud, J., Svendsen, J.-I., Lohmann, G., 2021. A new global ice sheet reconstruction for the  
589 past 80 000 years. *Nat. Commun.* 12, 1199.

590 Gregory, J.M., Griffies, S.M., Hughes, C.W., Lowe, J.A., Church, J.A., Fukimori, I., Gomez, N.,  
591 Kopp, R.E., Landerer, F., Le Cozannet, G., Ponte, R.M., Stammer, D., Tamisiea, M.E., van de  
592 Wal, R.S.W., 2019. Concepts and Terminology for Sea Level: Mean, Variability and Change,  
593 Both Local and Global. *Surv. Geophys.* 40, 1251-1289.

594 Hill, A.M., Milne, G.A., Kuchar, J., Ranalli, G., 2019. Sensitivity of glacial isostatic adjustment  
595 to a partially molten layer at 410 km depth. *Geophys. J. Int.* 216, 1538-1548.

596 Ivins, E.R., Caron, L., Adhikari, S., Larour, E., 2022. Notes on a compressible extended Burgers  
597 model of rheology. *Geophys. J. Int.* 228, 1975-1991.

598 Ivins, E.R., James, T.S., Wahr, J., Schrama, E.J.O., Landerer, F.W., Simon, K.M., 2013.  
599 Antarctic contribution to sea level rise observed by GRACE with improved GIA correction. *J.*  
600 *Geophys. Res. Solid Earth* 118, 3126-3141.

601 Ivins, E.R., van der Wal, W., Wiens, D.A., Lloyd, A.J., Caron, L., 2021. Antarctic upper mantle  
602 rheology. *Geological Society of London, Memoirs* 56.

603 Kang, K.X., Zhong, S.J., Geruo, A., Mao, W., 2022. The effects of non-Newtonian rheology in  
604 the upper mantle on relative sea level change and geodetic observables induced by glacial  
605 isostatic adjustment process. *Geophys. J. Int.* 228, 1887-1906.

606 Karato, S.-i., 2008. *Deformation of Earth Materials: An Introduction to the Rheology of Solid*  
607 *Earth.* Cambridge University Press, Cambridge.

608 Kendall, R.A., Mitrovica, J.X., Milne, G.A., 2005. On post-glacial sea level - II. Numerical  
609 formulation and comparative results on spherically symmetric models. *Geophys. J. Int.* 161, 679-  
610 706.

611 Lambeck, K., Purcell, A., Zhao, S., 2017. The North American Late Wisconsin ice sheet and  
612 mantle viscosity from glacial rebound analyses. *Quat. Sci. Rev.* 158, 172-210.

613 Lambeck, K., Rouby, H., Purcell, A., Sun, Y., Sambridge, M., 2014. Sea level and global ice  
614 volumes from the Last Glacial Maximum to the Holocene. *Proc. Natl. Acad. Sci. U.S.A.* 111,  
615 15296-15303.

616 Lambeck, K., Smither, C., Johnston, P., 1998. Sea-level change, glacial rebound and mantle  
617 viscosity for northern Europe. *Geophys. J. Int.* 134, 102-144.

618 Lambeck, K., Yokoyama, Y., Purcell, T., 2002. Into and out of the Last Glacial Maximum: sea-  
619 level change during Oxygen Isotope Stages 3 and 2. *Quat. Sci. Rev.* 21, 343-360.

620 Latychev, K., Mitrovica, J.X., Tromp, J., Tamisiea, M.E., Komatitsch, D., Christara, C.C., 2005.  
621 Glacial isostatic adjustment on 3-D Earth models: a finite-volume formulation. *Geophys. J. Int.*  
622 161, 421-444.

623 Lau, H.C.P., Austermann, J., Holtzman, B.K., Havlin, C., Lloyd, A.J., Book, C., Hopper, E.,  
624 2021. Frequency Dependent Mantle Viscoelasticity via the Complex Viscosity: Cases From  
625 Antarctica. *J. Geophys. Res. Solid Earth* 126, e2021JB022622.

626 Lau, H.C.P., Mitrovica, J.X., Austermann, J., Crawford, O., Al-Attar, D., Latychev, K., 2016.  
627 Inferences of mantle viscosity based on ice age data sets: Radial structure. *J. Geophys. Res. Solid*  
628 *Earth* 121, 6991-7012.

629 Lecavalier, B.S., Tarasov, L., 2021. History matching analysis of the Antarctic ice sheet  
630 evolution over the last glacial cycle, in: Austermann, J., Simms, A.R. (Eds.), *PALSEA-SERCE*  
631 *virtual workshop: Improving understanding of ice sheet and solid earth processes driving paleo*  
632 *sea level change*, p. 13.

633 Li, T.H., Wu, P., Steffen, H., Wang, H.S., 2018. In search of laterally heterogeneous viscosity  
634 models of glacial isostatic adjustment with the ICE-6G\_C global ice history model. *Geophys. J.*  
635 *Int.* 214, 1191-1205.

636 Li, T.H., Wu, P., Wang, H.S., Steffen, H., Khan, N.S., Engelhart, S.E., Vacchi, M., Shaw, T.A.,  
637 Peltier, W.R., Horton, B.P., 2020. Uncertainties of Glacial Isostatic Adjustment Model  
638 Predictions in North America Associated With 3D Structure. *Geophys. Res. Lett.* 47,  
639 e2020GL087944.

640 Love, R., Milne, G.A., Tarasov, L., Engelhart, S.E., Hijma, M.P., Latychev, K., Horton, B.P.,  
641 Tornqvist, T.E., 2016. The contribution of glacial isostatic adjustment to projections of sea-level  
642 change along the Atlantic and Gulf coasts of North America. *Earth's Future* 4, 440-464.

643 Melini, D., Spada, G., 2019. Some remarks on Glacial Isostatic Adjustment modelling  
644 uncertainties. *Geophys. J. Int.* 218, 401-413.

645 Miller, G.H., Wolfe, A.P., Steig, E.J., Sauer, P.E., Kaplan, M.R., Briner, J.P., 2002. The  
646 Goldilocks dilemma: big ice, little ice, or “just-right” ice in the Eastern Canadian Arctic. *Quat.*  
647 *Sci. Rev.* 21, 33-48.

648 Milne, G.A., Latychev, K., Schaeffer, A., Crowley, J.W., Lecavalier, B.S., Audette, A., 2018.  
649 The influence of lateral Earth structure on glacial isostatic adjustment in Greenland. *Geophys. J.*  
650 *Int.* 214, 1252-1266.

651 Mitrovica, J.X., Milne, G.A., 2003. On post-glacial sea level: I. General theory. *Geophys. J. Int.*  
652 154, 253-267.

653 Mitrovica, J.X., Wahr, J., Matsuyama, I., Paulson, A., 2005. The rotational stability of an ice-age  
654 earth. *Geophys. J. Int.* 161, 491-506.

655 Mix, A.C., Bard, E., Schneider, R., 2001. Environmental processes of the ice age: land, oceans,  
656 glaciers (EPILOG). *Quat. Sci. Rev.* 20, 627-657.

657 Nakada, M., Lambeck, K., 1989. Late Pleistocene and Holocene sea-level change in the  
658 Australian region and mantle rheology. *Geophys. J. Int.* 96, 497-517.

659 Nakada, M., Okuno, J., Lambeck, K., Purcell, A., 2015. Viscosity structure of Earth's mantle  
660 inferred from rotational variations due to GIA process and recent melting events. *Geophys. J. Int.*  
661 202, 976-992.

662 Nakada, M., Okuno, J., Yokoyama, Y., 2016. Total meltwater volume since the Last Glacial  
663 Maximum and viscosity structure of Earth's mantle inferred from relative sea level changes at  
664 Barbados and Bonaparte Gulf and GIA-induced  $\dot{J}_2$ . *Geophys. J. Int.* 204, 1237-1253.

665 Paulson, A., Zhong, S.J., Wahr, J., 2007. Inference of mantle viscosity from GRACE and relative  
666 sea level data. *Geophys. J. Int.* 171, 497-508.

667 Peltier, W.R., 2004. Global glacial isostasy and the surface of the ice-age earth: The ice-5G  
668 (VM2) model and GRACE. *Annu. Rev. Earth Planet. Sci.* 32, 111-149.

669 Peltier, W.R., Argus, D.F., Drummond, R., 2015. Space geodesy constrains ice age terminal  
670 deglaciation: The global ICE-6G\_C (VM5a) model. *J. Geophys. Res. Solid Earth* 120, 450-487.

671 Peltier, W.R., Fairbanks, R.G., 2006. Global glacial ice volume and Last Glacial Maximum  
672 duration from an extended Barbados sea level record. *Quat. Sci. Rev.* 25, 3322-3337.

673 Ranalli, G., 2001. Mantle rheology: radial and lateral viscosity variations inferred from  
674 microphysical creep laws. *J. Geodyn.* 32, 425-444.

675 Raymo, M.E., Kozdon, R., Evans, D., Lisiecki, L., Ford, H.L., 2018. The accuracy of mid-  
676 Pliocene  $\delta^{18}\text{O}$ -based ice volume and sea level reconstructions. *Earth-Sci. Rev.* 177, 291-302.

677 Ritsema, J., Deuss, A., van Heijst, H.J., Woodhouse, J.H., 2011. S40RTS: a degree-40 shear-  
678 velocity model for the mantle from new Rayleigh wave dispersion, teleseismic traveltimes and  
679 normal-mode splitting function measurements. *Geophys. J. Int.* 184, 1223-1236.

680 Roy, K., Peltier, W.R., 2017. Space-geodetic and water level gauge constraints on continental  
681 uplift and tilting over North America: regional convergence of the ICE-6G\_C (VM5a/VM6)  
682 models. *Geophys. J. Int.* 210, 1115-1142.

683 Schaeffer, A.J., Lebedev, S., 2013. Global shear speed structure of the upper mantle and  
684 transition zone. *Geophys. J. Int.* 194, 417-449.

685 Simms, A.R., Lisiecki, L., Gebbie, G., Whitehouse, P.L., Clark, J.F., 2019. Balancing the last  
686 glacial maximum (LGM) sea-level budget. *Quat. Sci. Rev.* 205, 143-153.

687 Simon, K.M., Riva, R.E.M., 2020. Uncertainty Estimation in Regional Models of Long-Term  
688 GIA Uplift and Sea Level Change: An Overview. *J. Geophys. Res. Solid Earth* 125,  
689 e2019JB018983.

690 Steffen, R., Audet, P., Lund, B., 2018. Weakened Lithosphere Beneath Greenland Inferred From  
691 Effective Elastic Thickness: A Hot Spot Effect? *Geophys. Res. Lett.* 45, 4733-4742.

692 Tarasov, L., Dyke, A.S., Neal, R.M., Peltier, W.R., 2012. A data-calibrated distribution of  
693 deglacial chronologies for the North American ice complex from glaciological modeling. *Earth*  
694 *Planet. Sci. Lett.* 315-316, 30-40.

695 van der Wal, W., Barnhoorn, A., Stocchi, P., Gradmann, S., Wu, P., Drury, M., Vermeersen, B.,  
696 2013. Glacial isostatic adjustment model with composite 3-D Earth rheology for Fennoscandia.  
697 *Geophys. J. Int.* 194, 61-77.

698 Waelbroeck, C., Labeyrie, L., Michel, E., Duplessy, J.C., McManus, J.F., Lambeck, K., Balbon,  
699 E., Labracherie, M., 2002. Sea-level and deep water temperature changes derived from benthic  
700 foraminifera isotopic records. *Quat. Sci. Rev.* 21, 295-305.

701 Whitehouse, P.L., Bentley, M.J., Le Brocq, A.M., 2012. A deglacial model for Antarctica:  
702 geological constraints and glaciological modelling as a basis for a new model of Antarctic glacial  
703 isostatic adjustment. *Quat. Sci. Rev.* 32, 1-24.

704 Wu, P., Wang, H.S., 2008. Postglacial isostatic adjustment in a self-gravitating spherical earth  
705 with power-law rheology. *J. Geodyn.* 46, 118-130.

706 Yokoyama, Y., Esat, T.M., Thompson, W.G., Thomas, A.L., Webster, J.M., Miyairi, Y.,  
707 Sawada, C., Aze, T., Matsuzaki, H., Okuno, J., Fallon, S., Braga, J.-C., Humblet, M., Iryu, Y.,  
708 Potts, D.C., Fujita, K., Suzuki, A., Kan, H., 2018. Rapid glaciation and a two-step sea level  
709 plunge into the Last Glacial Maximum. *Nature* 559, 603-607.

710 Yokoyama, Y., Lambeck, K., De Deckker, P., Johnston, P., Fifield, L.K., 2000. Timing of the  
711 Last Glacial Maximum from observed sea-level minima. *Nature* 406, 713-716.

712 Yousefi, M., Milne, G.A., Latychev, K., 2021. Glacial isostatic adjustment of the Pacific Coast  
713 of North America: the influence of lateral Earth structure. *Geophys. J. Int.* 226, 91-113.

714